

Rotation Mechanism of Molecular Motor V_1 -ATPase Studied by Multiscale Molecular Dynamics Simulation

Yuta Isaka,¹ Toru Ekimoto,¹ Yuichi Kokabu,¹ Ichiro Yamato,² Takeshi Murata,^{3,4} and Mitsunori Ikeguchi^{1,*}

¹Graduate School of Medical Life Science, Yokohama City University, Tsurumi, Yokohama, Japan; ²Department of Biological Science and Technology, Tokyo University of Science, Katsushika-ku, Tokyo, Japan; ³Department of Chemistry, Graduate School of Science, Chiba University, Inage, Chiba, Japan; and ⁴JST, PRESTO, Inage, Chiba, Japan

ABSTRACT *Enterococcus hirae* V_1 -ATPase is a molecular motor composed of the A_3B_3 hexamer ring and the central stalk. In association with ATP hydrolysis, three catalytic AB pairs in the A_3B_3 ring undergo conformational changes, which lead to a 120° rotation of the central stalk. To understand how the conformational changes of three catalytic pairs induce the 120° rotation of the central stalk, we performed multiscale molecular dynamics (MD) simulations in which coarse-grained and all-atom MD simulations were combined using a fluctuation matching methodology. During the rotation, a catalytic AB pair spontaneously adopted an intermediate conformation, which was not included in the initial inputs of the simulations and was essentially close to the “bindable-like” structure observed in a recently solved crystal structure. Furthermore, the creation of a space between the bindable-like and tight pairs was required for the central stalk to rotate without steric hindrance. These cooperative rearrangements of the three catalytic pairs are crucial for the rotation of the central stalk.

INTRODUCTION

Vacuolar ATPase (V-ATPase) is located in membranes and functions as a proton (or ion) pump coupled to adenosine triphosphate (ATP) hydrolysis (1–11). V-ATPase regulates the acidic environment in organelles and membrane vesicles; therefore, its function is related to various cellular activities, such as bone resorption by osteoclasts, the pH homeostasis of renal intercalated cells, the membrane trafficking processes of receptor-mediated endocytosis, protein degradation, and the tumor metastasis of cancer cells. Because the disorder of acidification causes diseases such as osteoporosis, cancer, neurological disorders, and metabolic diseases, V-ATPase is a potential pharmaceutical drug target (1–4). V-ATPase is composed of the V_O and V_1 moieties connected to stators (Fig. 1 A): the V_O moiety is a proton (or ion) pump embedded in membranes and is composed of several subunits (a-subunit, c-ring, and d-subunit). The soluble V_1 moiety (V_1 -ATPase) functions as a motor protein coupled to ATP hydrolysis. The central stalk (D and F subunits) penetrates the center of the A_3B_3 hex-

amer ring, which has an alternating arrangement of three catalytic A subunits and three noncatalytic B subunits. An ATP-binding site is located at the interface of the AB pair, and ATP hydrolysis occurs at each site in succession. Then, the A_3B_3 ring undergoes conformational changes. The conformational changes induce a rotation of the central stalk, and the rotation leads to the transportation of a proton (or ion) in the V_O moiety.

A series of V_1 -ATPase structures of *Enterococcus hirae* V_1 -ATPase have been revealed by x-ray crystallography (12,13). *E. hirae* V-ATPase is a prokaryotic V-ATPase, not a eukaryotic V-ATPase described above. However, *E. hirae* V-ATPase physiologically transports ions (5–9), similarly to eukaryotic V-ATPases, and the subunits of *E. hirae* V-ATPase are homologous to the corresponding subunits of eukaryotic V-ATPases. Therefore, we believe that *E. hirae* V-ATPase is a homolog of eukaryotic V-ATPases.

Changing the conditions of nucleotides, Murata et al. (12,13) have solved three crystal structures of *E. hirae* V-ATPase. For the binding patterns of the nucleotides at the three sites of the A_3B_3 ring, these crystal structures are regarded as three different states of an ATP hydrolysis, i.e., “the catalytic dwell” ($2_{ATP}V_1$, Fig. 1 B), “the ATP-binding dwell” ($2_{ADP}V_1$, Fig. 1 C), and “the ADP-release

Submitted September 23, 2016, and accepted for publication January 30, 2017.

*Correspondence: ike@tsurumi.yokohama-cu.ac.jp

Editor: Hiroyuki Noji

<http://dx.doi.org/10.1016/j.bpj.2017.01.029>

© 2017 Biophysical Society.

This is an open access article under the CC BY-NC-ND license (<http://creativecommons.org/licenses/by-nc-nd/4.0/>).



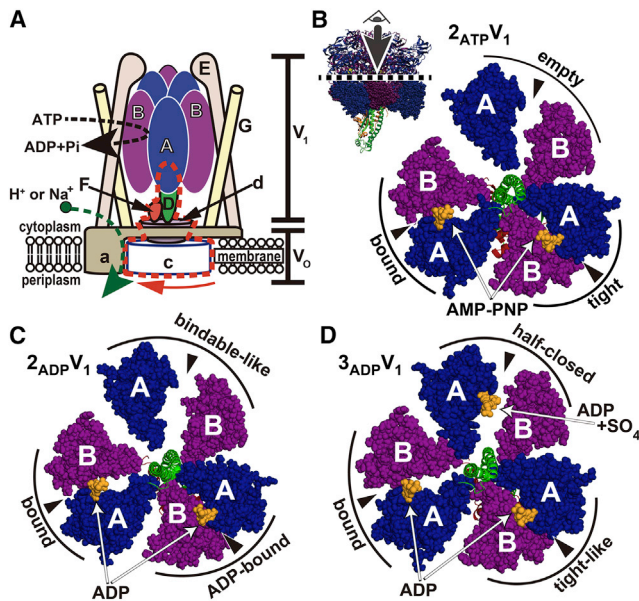


FIGURE 1 Structures of V-ATPase. A schematic view of the V-ATPase structure is shown in (A). In (B)–(D) three crystal structures of V_1 -ATPase (PDB ID: 3VR6, 5KNB, and 5KNC) (12,13) are drawn in a sliced view from the N-terminal domain.

dwel” ($3_{ADP}V_1$, Fig. 1 D). In the crystal structures, the three catalytic AB pairs in the A_3B_3 ring adopt different conformations, depending on nucleotides at the three ATP-binding sites. In the $2_{ATP}V_1$ crystal structure (12), the three AB pairs are termed the “empty,” “bound,” and “tight” pairs, respectively. No nucleotide is bound to the empty pair, and an ATP analog (AMP-PNP) is bound to the bound pair and to the tight pair. Due to the tightly packed interface of the tight pair, the tight pair is regarded as the dwelling structure just before ATP hydrolysis. In contrast, the $2_{ADP}V_1$ crystal structure (13) is regarded as the conformation just after the phosphate release from the tight pair. The three AB pairs for $2_{ADP}V_1$ are termed the “bindable-like,” “bound,” and “ADP-bound” pairs. Because phosphate release occurs, the ADP-bound pair has a looser interface than that of the tight pair. No nucleotide is bound to the bindable-like pair in the same manner as the empty pair; in contrast, the bindable-like pair has a wider interface than that of the empty pair and has affinity for the ATP binding. The interface of the nucleotide-binding site in the bindable-like pair is quite similar to that of the “bindable” pair observed in the crystal structure of the A_3B_3 ring without the central stalk and any nucleotides (PDB ID: 3VR2) (12). The bindable pair is regarded as the state of waiting for ATP binding; therefore, the bindable-like pair is also considered to be a dwelling structure for ATP binding (13). The $3_{ADP}V_1$ crystal structure (13) is regarded as the conformation after the ATP binding at the bindable-like pair of the $2_{ADP}V_1$ crystal structure. The three pairs are termed the “half-closed,” “bound,” and “tight-like” pairs. An adenosine diphosphate (ADP) is bound to all three pairs; in addition, a sulfate is bound to

the half-closed pair. The half-closed pair is regarded as an intermediate state on the way of the conformational change from the bindable-like to the bound pair after ATP binding, and the tight-like pair is considered the dwelling structure before ADP release. However, it is not clear whether the conformations of the three pairs in the $3_{ADP}V_1$ crystal structure exist together in physiological conditions, because the $3_{ADP}V_1$ crystal structure was crystallized under ADP surplus conditions (13).

The rotational behavior of the central stalk of *E. hirae* V_1 and the corresponding rotary catalysis have been analyzed by single-molecule high-speed imaging (14–17). A 360° rotation occurs in milliseconds in association with three ATP hydrolysis events and is achieved by a three-pause rotation consisting of 120° intervals. The 120° rotation that occurs in association with ATP hydrolysis does not include substeps, unlike the situation of F_1 -ATPase (18), suggesting that the rotation mechanism of V_1 -ATPase differs from that of F_1 -ATPase (19–26).

A possible model of the rotation coupled with an ATP hydrolysis has been proposed that combines insights from x-ray crystallography and single-molecule high-speed imaging (12,13). In association with ATP hydrolysis, the A_3B_3 ring undergoes a series of conformational changes: specifically, successive changes among the $2_{ATP}V_1$, $2_{ADP}V_1$, $3_{ADP}V_1$, and $2_{ATP}V_1$ structures, where the last $2_{ATP}V_1$ structure is a 120° rotated structure of the initial $2_{ATP}V_1$ structure. Following the conformational changes of the A_3B_3 ring, the central stalk rotates 120° . In the process, the empty pair at the initial state changes its conformation to the bindable-like, half-closed, and then bound structure. However, in this model, a simple morphing among the three crystal structures is assumed. Such a simple interpolation among them suffers from a severe steric hindrance between the central stalk and the B subunit in the bindable-like pair during the rotation (13). Therefore, for the rotation of the central stalk, dynamic rearrangements of the three AB pairs are required to avoid steric hindrance. In addition, it is not clear whether the intermediate conformations, such as the bindable-like and half-closed pairs, are necessary for the rotation and how the conformational changes of three AB pairs cooperate with each other during the rotation.

To understand the mechanism of the 120° rotation structurally, we studied the cooperative motions among the three AB pairs and the central stalk using molecular dynamics (MD) simulations. According to the single-molecule experiments, the 120° rotation occurs in a timescale on the order of milliseconds, which is beyond the timescale of all-atom (AA) MD simulations. To treat the long time-scale dynamics, we adopted multiscale MD simulations in which AA-MD and coarse-grained (CG) MD simulations were combined using the fluctuation matching methodology, which is a method of turning the parameters of CG-MD simulations. In principle, the parameters of CG-MD simulations are arbitrary, and the dynamics of CG

residues strongly depend on how the parameters are tuned. In our study, the fluctuations of CG residues around a minimum on a free energy surface were matched to those of AA-MD simulations at an equilibrium state near the crystal structure. Then, using the CG-MD simulation, we successfully reproduced a 120° rotation and observed the detailed behavior during conformational changes of the three AB pairs through intermediate states during the rotation. The intermediate state was necessary to avoid the steric hindrance.

MATERIALS AND METHODS

Modeling and preparation of the solution system

First, for the 2_{ATP}V₁ (PDB ID: 3VR6) (12) and 2_{ADP}V₁ (PDB ID: 4ZD7) (13) crystal structures, missing residues (A subunit in the tight pair (A_{tight}): 279–282, D: 69–77, 84–86, and 109–127 for 2_{ATP}V₁; D: 62–86, 110–126, and 207, F: 2, 3, and 99–103 for 2_{ADP}V₁) were modeled using MODELER (27) as follows. For the A_{tight} subunit, the A subunit in the bound pair structure of 2_{ATP}V₁ was used as a template. For the D and F subunits, the crystal structures of the D and F subunits (PDB ID: 3AON) (10) were used as a template. Because the 2_{ATP}V₁ crystal structure corresponds to the catalytic dwell state, AMP-PNP molecules in the tight and bound pairs were replaced with ATP molecules. Because the 2_{ADP}V₁ crystal structure is regarded as the ATP-binding dwell state, the ADP molecule in the bound pair was replaced with an ATP molecule. The lengths of the N- and C-termini of the A and B subunits were uniform: 1–586 residues were used for the A subunit, and 4–454 residues used for the B subunit.

The missing hydrogen atoms were added in accordance with the topology in the CHARMM27 force field (28–32). The N- and C-termini were set as NH₃⁺ and COO⁻, respectively. The protein was placed at the center of a rectangular cell, and the cell was filled with water molecules. The thickness of the water layer was 15 Å from the long axis of proteins, and the MD unit cells were (151.60, 155.60, and 177.79 Å) for the 2_{ATP}V₁ system and (159.83, 156.23, and 183.56 Å) for the 2_{ADP}V₁ system.

All-atom molecular dynamics simulations

All AA-MD simulations were performed using the MD program package MARBLE (33) with the CHARMM27/CMAP force field (28–32) and the TIP3P water model (34). The isothermal-isobaric (*NPT*) ensemble was adopted with periodic boundary conditions. The temperature and pressure were set at 300 K and 1 atm, respectively. Bond lengths and angles involving hydrogen atoms were constrained using the partial rigid-body integrator at the 2 fs time step. The *NPT* ensemble was generated using the extended-system approach (33,35). The electrostatic interaction was handled by the particle-mesh Ewald method (36). The Lennard-Jones potential was smoothly truncated to zero over the range 8–10 Å (37,38). Na⁺ and Cl⁻ ions were added so that the ion density was 150 mM, and counterions were added to keep the total charge neutral. Before the production run, a 2000-step minimization using the steepest descent method, a heating simulation from 1 to 300 K over 100 ps with heavy atom restraints, and a 100 ps simulation to gradually remove the restraints were consecutively executed. The production run was performed for 100 ns.

Coarse-grained molecular dynamics simulations

All CG-MD simulations were performed using the program package CafeMol (39). The minimized structure of the 2_{ATP}V₁ crystal structure in solution determined by the AA-MD simulation was adopted for the initial structure. Each amino-acid residue was simplified into one bead, and beads

were located at the C α atoms of residues. The AICG model (40) was used to set the parameters for bonded and nonbonded interactions. For the fluctuation matching protocol, we performed multiple CG-MD simulations with various values of temperature (T_{CG}) in the range from 175 to 275 K for 1.0×10^7 steps, and the snapshots were saved for every 1000 steps (10,000 snapshots in total). The root-mean-square fluctuations (RMSF) and correlation matrices were calculated from all snapshots for each simulation. The RMSF values calculated from the CG-MD simulation were compared with those of the AA-MD simulation. The RMSF deviation between the AA- and CG-MD simulations was estimated as follows:

$$\Delta RMSF_{AA-CG}(T_{CG}) = \sqrt{\sum_i (RMSF_{AA-MD,i} - RMSF_{CG-MD,i}(T_{CG}))^2}, \quad (1)$$

where $RMSF_{AA/CG-MD,i}$ is the RMSF of the i -th residue calculated by the AA/CG-MD simulation, and the summation was performed for residues in the A₃B₃ subunits and the 1–39 and 160–207 residues of the D subunit. The RMSF results indicated that $T_{CG} = 240$ K provided the best agreement with the AA-MD simulation at 300 K. Thus, $T_{CG} = 240$ K was used for the following simulations.

To simulate a 120° rotation of the central stalk, a multiple-Go model (41) was used. In the multiple-Go model, a double-well potential was adopted. The two minima of the double-well potential were set at the structures before and after ATP hydrolysis corresponding to the 2_{ATP}V₁ crystal structure and its 120° rotated structure, respectively. The two structures in the CG representation are shown in Fig. 2. Hereafter, to represent conformational changes clearly, we call the three subunit pairs as A_IB_I, A_{II}B_{II}, and A_{III}B_{III}, respectively, and describe their states as shown in the interfaces of the AB pairs in Fig. 2. For a structural transition between the two basins, the height of the barrier was modulated by setting a function (41) that smoothly connected the two basins. The parameter of the function, “ Δ ,” was set to 800. In addition, as described in a previous work (42) that used CafeMol with the multiple-Go model, the effect of chemical processes, such as ligand binding, was mimicked using the energy gap between the states corresponding to energy minima. Therefore, to mimic an ATP hydrolysis event in the present calculation, the energy of the after-hydrolysis structure was set to a smaller value than that of the prehydrolysis structure. Here, the energy gap between these structures was set to 200. Using the parameters ($\Delta = 800$, the energy gap = 200), we repeated the CG-MD simulations 11 times using the multiple-Go model for 1.0×10^7 steps.

The parameters ($\Delta = 800$, energy gap = 200) were determined after trial simulations. For too small Δ , the barrier between two basins is high, resulting in no transitions between two basins. In contrast, for too large Δ , the

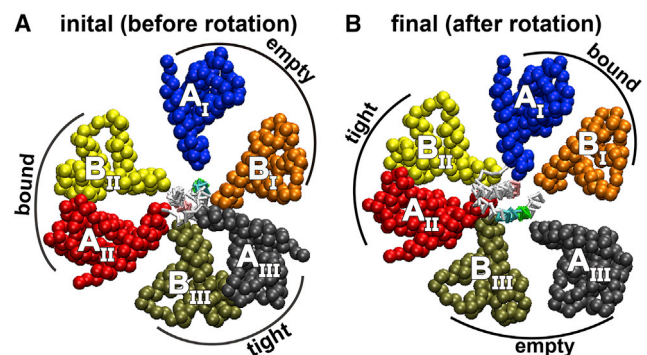


FIGURE 2 Initial and final structures of the A₃B₃ subunits for CG-MD simulations. Three different subunit pairs are referred to as A_IB_I, A_{II}B_{II}, and A_{III}B_{III}, respectively. The structures of (A) and (B) correspond to the initial and final structures at the two minima in the multiple-Go potential, respectively.

barrier disappears, and an artificial local minimum appears at the midpoint between two basins. From CG-MD simulations changing Δ from 200 to 2000, we determined an adequate value for Δ . Similarly, when the too small energy gap is used, no rotation occurred. For the too large energy gap, too quick transitions took place. From CG-MD simulations changing the energy gap from 160 to 240, we chose an adequate value for the energy gap.

Correlation matrix

RMSF values were calculated as $\sqrt{\langle (R_i - \langle R_i \rangle)^2 \rangle}$, where R_i is the position of i -th C α atom, and $\langle X \rangle$ represents the time average of X . RMSF represents the magnitude of the residue fluctuations. In flexible regions, such as loops, the RMSF values are large, and in rigid regions, such as helices, the RMSF values are small. In the present calculation, RMSF values were calculated from the last 50 ns trajectory of the AA-MD simulation for the $2_{\text{ATP}}V_1$ crystal structure and were also calculated from the whole trajectory of the CG-MD simulation. The C α atoms of the A₃B₃ and D subunits were used except for the protruded regions of the D subunit (residues 40–159).

The correlation matrix C_{ij} was calculated by the following:

$$C_{ij} = \frac{\langle (R_i - \langle R_i \rangle)^2 (R_j - \langle R_j \rangle) \rangle}{\sqrt{\langle (R_i - \langle R_i \rangle)^2 \rangle \langle (R_j - \langle R_j \rangle)^2 \rangle}}, \quad (2)$$

and indicates the degree of correlated fluctuations between residues. For example, the value of 1 represents a fully correlated movement, and a value of ~ 0 represents no correlations. An area with high correlations indicates a domain motion. In the present calculation, the correlation matrix was calculated for the same trajectories as used in the RMSF calculation.

Estimation of rotation angle

The rotation angle for each snapshot was calculated as follows: first, a horizontal plane of a V_1 snapshot structure was determined. The horizontal plane was defined by the three centers of mass of the N-terminal domains of the three A subunits. Next, the direction of the central stalk was defined by two residues of the D subunit: D31 in the N-terminal helix and E161 in the C-terminal helix. Then, the vectors connecting D31 and E161 were projected onto the horizontal plane. The rotation angle between the projected vectors at steps N and $N + 1$ was evaluated, and the time evolution of the rotation angle was calculated by their summations.

RESULTS AND DISCUSSION

Fluctuation matching

To perform the multiscale MD simulation of V_1 -ATPase, first we conducted an AA-MD simulation from the $2_{\text{ATP}}V_1$ crystal structure in solution at 300 K. From the AA-MD simulation, the magnitudes of fluctuations of residues were estimated by the RMSF (Fig. 3). Independently of the AA-MD, CG-MD simulations were also performed at various temperatures (T_{CG}), and the RMSF was calculated for each T_{CG} . From a comparison with the RMSF for the AA-MD and CG-MD simulations, an appropriate T_{CG} was determined so that the RMSF at T_{CG} was similar to that of AA-MD at 300 K. When T_{CG} was set at 240 K, the RMSF of all A and B subunits in the CG-MD simulation were in good agreement with those in the AA-MD simulation

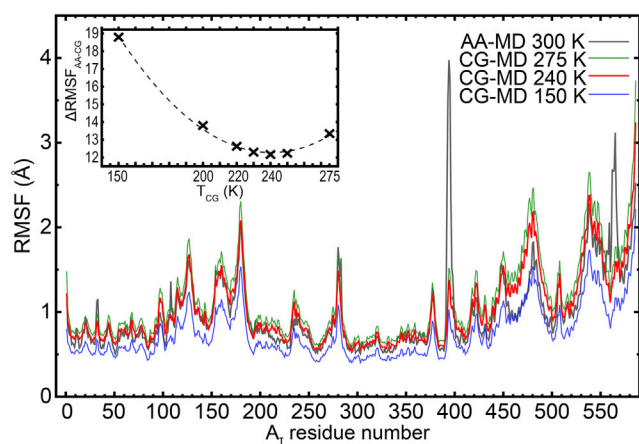


FIGURE 3 RMSF of the A subunit in the empty pair calculated from AA-MD simulations at 300 K and CG-MD simulations at 150, 240, and 275 K. The inset panel represents the RMSF deviation between the AA- and CG-MD simulations, with $\Delta\text{RMSF}_{\text{AA-CG}}$ plotted against T_{CG} .

(Figs. 3 and S1 in the Supporting Material), and their correlation coefficient was 0.815: the consistency between the CG- and AA-MD simulations was remarkable in the secondary-structure regions, indicating that the dynamics simulated in the two simulations were matched to one another. Using the fluctuation matching method, we could tune the parameters of the CG-MD simulation only using T_{CG} , and the temperature $T_{\text{CG}} = 240$ K was employed in the following calculations. This agreement between the CG and AA-MD fluctuations is not surprising because the force field of CG-MD employed here was designed on the basis of atomic interactions (the AICG model).

This fluctuation matching allowed us to perform CG-MD simulations involving the dynamics sampled in AA-MD simulations. In the present calculation, the fluctuation matching was performed using a quasi-stable state near the crystal structure. Namely, the fluctuations in the CG-MD simulations are close to those of the AA-MD simulations around a minimum of a potential surface corresponding to the crystal structure.

The 120° rotation of the central stalk in a multiple-Go model

To simulate the 120° rotation of the central stalk during ATP hydrolysis, a multiple-Go model (39,41–43) was used. The two minima on the multiple-Go potential were set at the structures before and after ATP hydrolysis corresponding to the $2_{\text{ATP}}V_1$ crystal structure and its 120° rotated structure, respectively (Fig. 2). The $2_{\text{ATP}}V_1$ crystal structure is regarded as a hydrolysis-waiting form, because the structure was crystallized in the presence of AMP-PNP. The two basins corresponding to the two structures were sufficiently separated, and a high barrier existed between them. For the transition between the two basins to occur, the height of the barrier was modulated by setting a function

(39,41–43) that smoothly connected the two basins. In addition, to mimic ATP hydrolysis, the minimum value for the after-hydrolysis structure was set at a lower value than that for the prehydrolysis structure. To date, the multiple-Go models have been successfully applied to various biomolecular systems involving large structural changes (39,41–43). Using the double-well potential, we performed CG-MD simulations at $T_{CG} = 240$ K and independently repeated 11 times. A rotation of the central stalk occurred in nine simulations, and the time dependence of the rotation angles during a simulation is illustrated in Fig. 4 A. As the simulation proceeded, the central stalk rotated from 0° to 120° (Movie S1). The rotation did not include any sub-steps, and the behavior is consistent with the single-molecule experiments (14–17).

Spontaneous emergence of the bindable-like structure

The intermediate states of the AB pair spontaneously emerged during the rotation, and the corresponding structure was essentially close to the bindable-like structure observed in the $2_{ADP}V_1$ crystal structure. To examine the conformational change of the AB pair, the time depen-

dence of the conformation was estimated by the RMSD from the empty, bound, bindable-like structures in the crystal structure. The RMSD of the A_1B_1 pair is illustrated in Fig. 4 B (see Fig. S2 for other pairs). The A_1B_1 pair adopted the empty structure in the initial structure. Before the 3520×10^3 step, the A_1B_1 pair remained in the empty structure and underwent a structural transition to the bindable-like structure. The RMSD of the A_1B_1 pair from the bindable-like crystal structure was the smallest from the 3520×10^3 to 3565×10^3 steps. The snapshot structure at the minimum RMSD (1.36 \AA) of the bindable-like structure was superimposed on the corresponding part in the $2_{ADP}V_1$ crystal structure (Fig. 4 D). The structure of the A_1B_1 pair from the CG-MD was in good agreement with that of the crystal structure. Additionally, in all the CG-MD simulations, the A_1B_1 pair adopted the bindable-like structure as shown in Fig. S3. This emergence of the bindable-like structure in the simulation is not trivial. In the simulation, the $2_{ADP}V_1$ crystal structure was not used as the initial structure. Further, the bindable-like structure was not on the pathway found by simple interpolation between the empty and bound structures. In fact, compared with the empty structure, the bindable-like structure exhibited a more open interface between A and B subunits.

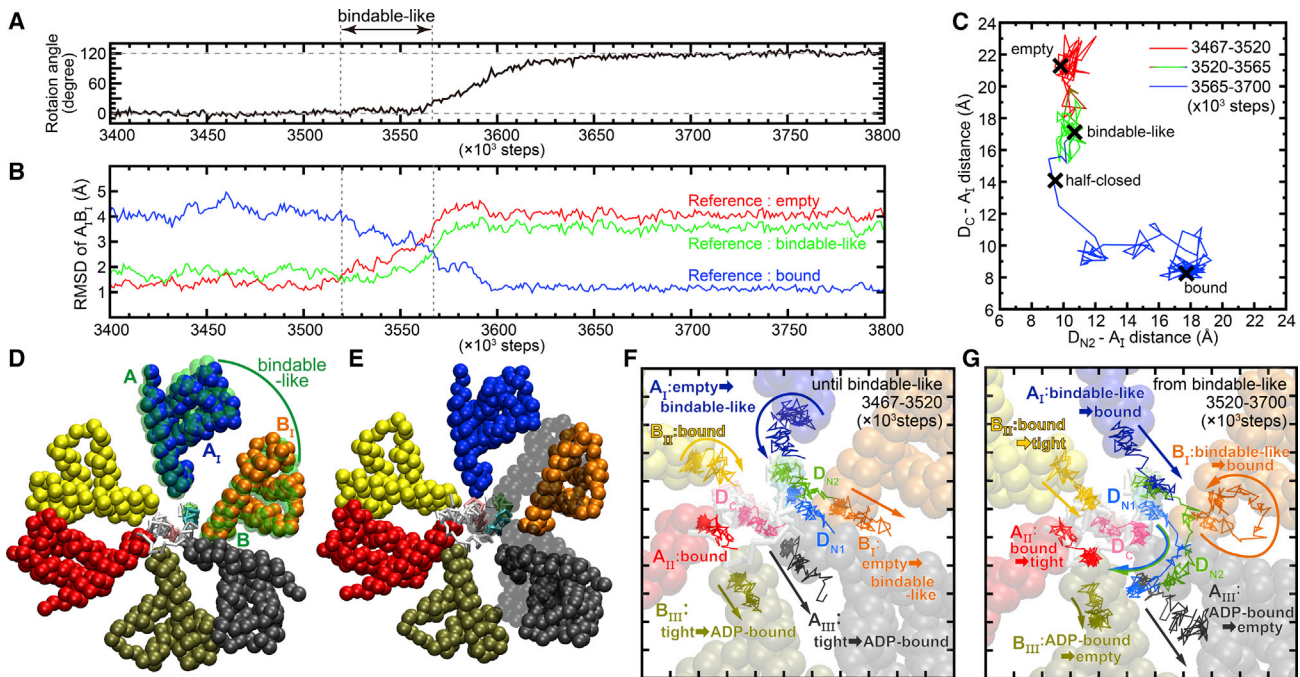


FIGURE 4 Rotation of the central stalk and structural rearrangements of the A_3B_3 subunits in V_1 -ATPase observed in a trajectory of a CG-MD simulation. The time evolution of the rotation angle of the stalk is shown in (A). The time evolution of the RMSD of the A_1B_1 pair from the empty, bindable-like, and bound structures in the crystal structures are compared in (B). A snapshot at the 3536×10^3 step in the CG-MD simulation is compared with the bindable-like structure of the crystal structure (PDB ID: 5KNB) (green) in (D). A snapshot at the 3565×10^3 step showing the large space between subunit A_{III} (black) and B_1 (orange) is illustrated in (E). For comparison of the space, the corresponding initial structures of subunits A_{III} and B_1 are shown in gray. The time evolution of the distances between the A_1 subunit and the N- and C-termini helices of the central stalk are plotted in (C). The trajectories of the C-terminal region for the 3467×10^3 –to 3520×10^3 steps and the 3520×10^3 to 3700×10^3 steps are drawn in (F) and (G), respectively. The trajectories correspond to the movement of the center of mass of the C-terminal regions: R475–L477 of subunit A, E384–S392 of subunit B, and the contacting regions of the helices in the central stalk (D_{N1} : T20–L29, D_{N2} : K30–Q39, and D_C : K162–M173 of subunit D).

Nevertheless, in our simulation, the bindable-like structure spontaneously emerged as an intermediate state during the 120° rotation.

The emergence of the bindable-like structure is reasonable from the viewpoint of molecular function. It has been considered that the incoming ATP can bind to the AB pair only when the AB pair adopts the bindable conformation (12). Even when V_1 -ATPase or the A_3B_3 ring including the empty conformation was crystallized under ATP analog surplus conditions, no electron densities corresponding to ATP were observed in the binding site of the empty pair. In contrast, when the A_3B_3 ring including the bindable conformation was crystallized with the addition of an ATP analog, the bindable pair underwent the conformational change to the bound pair (PDB ID: 3VR2). Because the nucleotide-binding site is quite similar between the bindable and bindable-like structures, the bindable-like structure is regarded as the same state as the bindable structure (13). Therefore, the bindable-like structure has ATP-binding ability, but the empty structure does not. Considering the ATP affinity, the emergence of the bindable-like structure is absolutely necessary for the incoming ATP to bind to the catalytic AB pair.

The conformational change from the empty to the bindable-like structure was attained by a separation of the A and B subunits in the empty pair and the cooperative rearrangements of the other two adjacent pairs. The movements of the C-terminal regions in all subunits (R475-L477 for subunit A, E384-S392 for subunit B) are shown in Fig. 4 F and correspond to the trajectories (3467×10^3 to 3520×10^3 steps) that occur until the emergence of the bindable-like structure. The structural change of the $A_I B_I$ pair from the empty to bindable-like structures was mainly achieved by a cooperative rearrangement of the $A_{III} B_{III}$ pair (the tight pair), as follows. First, the interface in the tight pair opened due to the ATP hydrolysis. Then, the A_{III} subunit moved outside and brought the B_I subunit in the same direction (Fig. 4 F) because of the interactions between the A_{III} and B_I subunits in the C-terminal regions. Thus, the B_I subunit moved toward the A_{III} subunit of the tight pair, resulting in a separation of the interface between the A_I and B_I subunits.

The cooperative rearrangement of the B_I and A_{III} pairs triggered the rotation of the central stalk. The contact region of the central stalk with the A_3B_3 ring was composed of the two helices corresponding to the N- and C-termini that were termed “ D_N ” and “ D_C ,” respectively (Fig. S4). The A_{III} subunit interacted with both D_N and D_C ; then, the outgoing movement of the A_{III} subunit caused a tilt of the central stalk in the same direction (Fig. 4 F). This tilt of the central stalk is also present in the $2_{ADP}V_1$ crystal structure, despite the fact that the crystal structure was not used as an input for the current CG-MD simulation. Following the tilt of the stalk, in the empty pair, the A_I subunit moved inward. The A_I subunit was approaching D_C while retaining the contact

distance between A_I and D_N (Fig. 4 F). During the movement, the interface site between A_I and D_N was shifted.

Avoidance of the steric hindrance of the stalk rotation

For a successful 120° rotation, in addition to the bindable-like structure, a large separation between the A_{III} and B_I subunits (black and orange, respectively, in Fig. 4 D) was necessary to avoid steric hindrance between the central stalk and the B_I subunit. In 2 of 11 simulations, no rotation was observed due to the steric hindrance between D_N and the B_I subunit, even after the $A_I B_I$ pair underwent the conformational change from the empty to the bindable-like structures (Fig. S5). In contrast, in the other simulations successfully exhibiting a 120° rotation, the space was spontaneously generated at the interface between the A_{III} and B_I subunits after the emergence of the bindable-like structure (Fig. 4 E; movements of the C-terminal regions are shown in Fig. 4 G and correspond to the following trajectories: (3520×10^3 to 3700×10^3 steps)). Next, due to the outward motion of the B_I subunit, the steric hindrance between the central stalk and the B_I subunit was avoided, leading to rotation of D_N into the space. The width of the space was estimated using the distance between the C-terminal regions in the A_{III} and B_I subunits (Fig. S6 A): the distance was ~ 13 Å before the rotation and ~ 22 Å after the 120° rotation, and the maximum distance was ~ 28 Å during the rotation, where the maximum distance was larger than those of the crystal structures. The large distance was observed in other eight simulations shown in Fig. S6 B, suggesting that the creation of the space always occurred in the rotation process.

After the conformational change of the $A_I B_I$ pair from the empty to the bindable-like structure described above, ATP binding induced the closing motion of the $A_I B_I$ pair from the bindable-like to the bound structure. During the conformational changes of the $A_I B_I$ pair, the A_I subunit switched from interacting with the central stalk at D_N to D_C . Before the rotation, the A_I subunit interacted only with D_N . As the empty structure changed to the bindable-like structure, the central stalk tilted, and then the A_I subunit moved to the space, leading to the interaction of the A_I subunit with both D_N and D_C (Fig. 4 F). This behavior was observed by the decrease in the distance between the A subunit and D_C (Fig. 4 C). As the bindable-like structure changed to the bound structure, the central stalk rotated toward the space generated by the separation of the A_{III} and B_I subunits, the distance between the A_I subunit and D_C decreased further, and finally the A_I subunit (Fig. 4 G) interacted only with D_C . These behaviors were analyzed by switching the contacts between the central stalk and the A subunit (Fig. S7). Interestingly, just before the generation of the space between the A_{III} and B_I subunits, the distance was in good agreement with the distance between the central stalk and

the A subunit of the half-closed AB pair in the $3_{ADP}V_1$ crystal structure (Fig. 4 C). In fact, the A subunit of half-closed pair contacts both D_N and D_C in the $3_{ADP}V_1$ crystal structure, suggesting that the bindable-like structure undergoes a closing motion upon nucleotide binding and that the interaction between the A subunit and the central stalk changed. The adjacent pair of the half-closed pair ($A_I B_I$) adopted the empty structure ($A_{III} B_{III}$) in the simulation snapshot rather than the tight-like structure of the $3_{ADP}V_1$ crystal structure. To avoid steric hindrance, the outward movement of the A_{III} subunit was necessary. Thus, the adjacent pair ($A_{III} B_{III}$) had to undergo the conformational change from the tight to the empty structure before the emergence of the half-closed structure. This result implies that the conformations of the three pairs in the $3_{ADP}V_1$ crystal structure do not emerge together during a 120° rotation.

A series of the conformational changes of the $A_3 B_3$ subunits are important for the rotation in the right direction. The creation of the space between the A_{III} and B_I subunits is crucial for the rotation of the central stalk. The space emerges in the correct direction of the rotation, and the central stalk rotates to fill the emerged space. Thus, the space acts as a steric constraint to ensure the correct rotation of the stalk. Because the creation of the space was achieved by the cooperative rearrangement of the $A_3 B_3$ subunits as described above, the rearrangement is an important factor for the correct rotation. This point is related to the result of the single-molecular experiment of F_1 -ATPase with changing the length of the stalk (44), showing that the axless F_1 -ATPase rotates in the correct direction. This result implies that an important factor for the correct rotation is the conformational changes of the $A_3 B_3$ ($\alpha_3 \beta_3$ in F_1 -ATPase) subunits. In addition, according to Baba et al. (45), amino-acid specific interactions between the stalk and the $A_3 B_3$ subunits are not required for the rotation of V_1 -ATPase, and the stalk rotates even though almost parts of the stalk are changed to the other protein adopting a coiled-coil structure. This result also implies that the important factor for the correct rotation may be included in the dynamics of the $A_3 B_3$ subunits rather than chemical and structural characteristics of the stalk itself.

Comparison of fluctuations in the AA- and CG-MD simulations

Finally, to confirm the dynamics revealed by the CG-MD simulations, we analyzed the fluctuations in the vicinity of the $2_{ATP}V_1$ and $2_{ADP}V_1$ crystal structures using AA-MD simulations. The CG-MD simulations indicated that the emergence of the bindable-like structure and the space between the bindable-like and tight pairs were necessary for the rotation of the central stalk. The bindable-like structure was generated by the cooperative movement of the A_{III} and B_I subunits in the same direction due to the interaction be-

tween these subunits. In the AA-MD simulation of the $2_{ATP}V_1$ crystal structure, highly correlated motions were observed between the C-terminal regions of the A subunit in tight pair (A_{tight}) and B subunit in the empty pair (B_{empty}) (Fig. S8 A). The correlated motions observed in AA-MD are consistent with the results of CG-MD simulation. Further, CG-MD indicated that after the emergence of the bindable-like structure, the B_I and A_{III} subunits must be separated to generate the space between the bindable-like and tight pairs. In the AA-MD simulation of the $2_{ADP}V_1$ crystal structure, the correlations in motion of the B subunit in the bindable-like pair and A subunit in the ADP-bound pair were smaller than those of the A_{tight} and B_{empty} subunits, suggesting that the A_{tight} and B_{empty} subunits did not move cooperatively after the emergence of the bindable-like structure (Fig. S8 B). These AA-MD results are consistent with the dynamics revealed by CG-MD simulations.

CONCLUSIONS

The mechanism underlying the rotation of the central stalk in V_1 -ATPase in conjunction with the cooperative rearrangements of the A and B subunits was investigated using multiscale MD simulations. A possible rotation mechanism associated with ATP hydrolysis is proposed (see Fig. 5; Movie S2) as delineated in the following. Although the nucleotides were not explicitly included in the CG-MD simulations, the binding states of nucleotides were estimated from the conformational changes of the subunits.

1. ATP hydrolysis occurs in the tight pair ($A_{III} B_{III}$), and a phosphate is released (Fig. 5, A and B).
2. The A_{III} subunit moves outside and pulls the B_I subunit in the same direction, resulting in widening the interface of the $A_I B_I$ pair (Fig. 5 B).
3. Once the A_I and B_I subunits of the empty pair separate from each other, the empty structure undergoes a conformational change to the bindable-like structure, which has affinity for ATP binding (Fig. 5, B and C).
4. Because the A_{III} subunit interacts with the central stalk, the central stalk is tilted in the same direction as the outside movement of the A_{III} subunit. Because of the tilt, the A_I subunit approaches the C-terminal helix of the central stalk (Fig. 5 C).
5. ATP binding occurs in the bindable-like structure ($A_I B_I$), and the bindable-like structure undergoes a conformational change to the bound structure. In addition, ADP release occurs in the tight pair ($A_{III} B_{III}$), and the A_{III} subunit moves further outward. (Fig. 5, C and D)
6. Due to the outward movement of the A_{III} subunit, the A_{III} and B_I subunits separate from each other, and then the N-terminal helix of the central stalk rotates to the space between the A_{III} and B_I subunits. As the B_I subunit moves further outward, the space between the B_I and A_{III} subunits widens more. The space avoids the steric

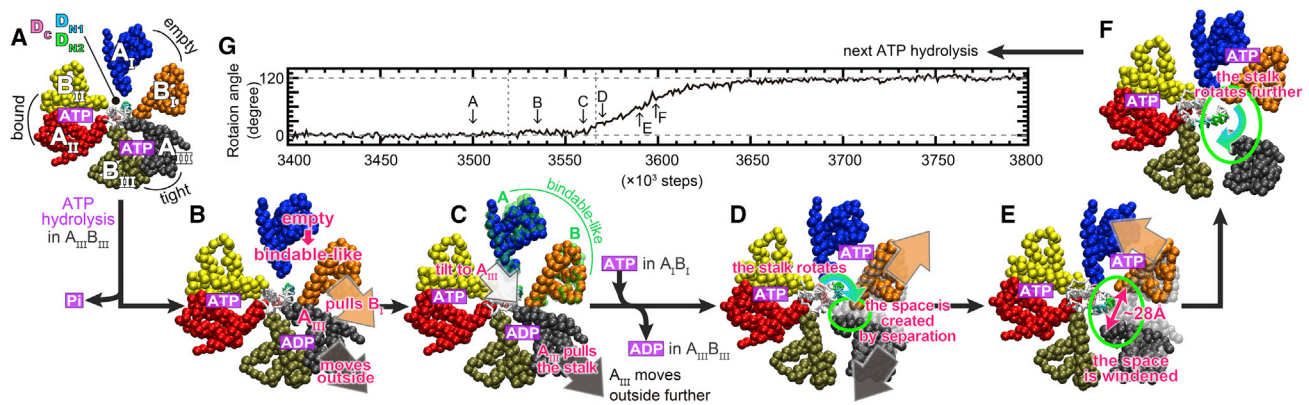


FIGURE 5 A model of the ATP hydrolysis processes during the 120° rotation. A 120° rotation occurred as the system progressed through each structure shown in (A)–(F). The corresponding steps for the (A)–(F) structures along the 120° rotation are represented in (G).

hindrance between the central stalk and the B₁ subunit (Fig. 5, D and E).

- During the structural change from the bindable-like to the bound structure (A₁B₁), the A₁ subunit switches its interaction partner on the central stalk. In the bindable-like structure, the A₁ subunit interacts only with the N-terminal helix of the stalk. On the pathway of the conformational changes, the A₁ subunit is transiently close to both the N- and C-terminal helices. Finally, in the bound structure, the A₁ subunit interacts only with the C-terminal helix (Fig. 5 E).
- During the structural change, the N-terminal helix of the central stalk further rotates to the space between A_{III} and B₁, and a 120° rotation is achieved (Fig. 5 F).

From these insights, we found that two conditions were necessary for a successful rotation of the central stalk: one is the emergence of the bindable-like structure (Fig. 5, B and C), and the other is the space between the A_{III} and B₁ subunits (Fig. 5, D and E). In particular, the space avoids the steric hindrance between the B₁ subunit and the central stalk, which was an unresolved problem in the previous model introduced by Murata et al. (12,13).

The cooperatively rearranging motion of the A₃B₃ subunits is key to the rotation in the right direction. The space emerges in the correct direction of the stalk rotation, and the central stalk rotates to enter the emerged space. Thus, the space acts as a steric constraint to ensure the correct rotation of the stalk. This implies that the important factor for the correct rotation is included in the dynamics of the A₃B₃ subunits rather than chemical and structural characteristics of the stalk itself as pointed in the single-molecule experiments of F₁- and V₁-ATPase (44,45).

Although the overall behavior of the rotation has been elucidated in this study, the nucleotide binding to the catalytic sites should be investigated in the next step. In this study, we did not explicitly deal with the nucleotide binding and dissociation of products during the ATP hydrolysis process. In the future, we will examine how the structural

change propagates from the binding pocket to the A₃B₃ ring. Furthermore, the different functions of V-ATPase in other species are interesting (18,46–49). It is known that *Thermus thermophilus* V-ATPase functions as an ATP synthase, suggesting that the central stalk may rotate in the opposite direction to that of *E. hirae* V-ATPase. Simulations will contribute to the elucidation of the difference in the V-ATPases of various species.

SUPPORTING MATERIAL

Eight figures and two movies are available at [http://www.biophysj.org/biophysj/supplemental/S0006-3495\(17\)30154-6](http://www.biophysj.org/biophysj/supplemental/S0006-3495(17)30154-6).

AUTHOR CONTRIBUTIONS

M.I. and T.M. designed research. Y.I., T.E., Y.K., and M.I. performed MD and analyzed data. Y.I., T.E., T.M., and M.I. wrote the article; and all authors discussed the results and contributed to the final version of the manuscript.

ACKNOWLEDGMENTS

This work was financially supported by the Platform for Drug Discovery, Informatics, and Structural Life Science from the Ministry of Education, Culture, Sports, Science and Technology (MEXT) and the Japan Agency for Medical Research and Development (AMED) to M.I.; Innovative Drug Discovery Infrastructure through Functional Control of Biomolecular Systems, Priority Issue 1 in Post-K Supercomputer Development from MEXT to M.I. (Project ID: hp150269 and hp160223); Grants-in-Aid for Scientific Research (No. 25291036) to M.I.; and RIKEN Dynamic Structural Biology Project to M.I.

REFERENCES

- Forgac, M. 2007. Vacuolar ATPases: rotary proton pumps in physiology and pathophysiology. *Nat. Rev. Mol. Cell Biol.* 8:917–929.
- Marshansky, V., and M. Futai. 2008. The V-type H⁺-ATPase in vesicular trafficking: targeting, regulation and function. *Curr. Opin. Cell Biol.* 20:415–426.

3. Cotter, K., L. Stransky, ..., M. Forgac. 2015. Recent insights into the structure, regulation, and function of the V-ATPases. *Trends Biochem. Sci.* 40:611–622.
4. Hayek, S. R., S. A. Lee, and K. J. Parra. 2014. Advances in targeting the vacuolar proton-translocating ATPase (V-ATPase) for anti-fungal therapy. *Front. Pharmacol.* 5:4.
5. Murata, T., I. Yamato, ..., J. E. Walker. 2005. Structure of the rotor of the V-Type Na⁺-ATPase from *Enterococcus hirae*. *Science*. 308:654–659.
6. Murata, T., I. Yamato, ..., S. Iwata. 2008. Ion binding and selectivity of the rotor ring of the Na⁺-transporting V-ATPase. *Proc. Natl. Acad. Sci. USA*. 105:8607–8612.
7. Murata, T., K. Igarashi, ..., I. Yamato. 2000. Na⁺ binding of V-type Na⁺-ATPase in *Enterococcus hirae*. *J. Biol. Chem.* 275:13415–13419.
8. Mizutani, K., M. Yamamoto, ..., T. Murata. 2011. Structure of the rotor ring modified with N,N'-dicyclohexylcarbodiimide of the Na⁺-transporting vacuolar ATPase. *Proc. Natl. Acad. Sci. USA*. 108:13474–13479.
9. Arai, S., I. Yamato, ..., T. Murata. 2009. Reconstitution in vitro of the catalytic portion (NtpA3-B3-D-G complex) of *Enterococcus hirae* V-type Na⁺-ATPase. *Biochem. Biophys. Res. Commun.* 390:698–702.
10. Saijo, S., S. Arai, ..., T. Murata. 2011. Crystal structure of the central axis DF complex of the prokaryotic V-ATPase. *Proc. Natl. Acad. Sci. USA*. 108:19955–19960.
11. Zhao, J., S. Benlekber, and J. L. Rubinstein. 2015. Electron cryomicroscopy observation of rotational states in a eukaryotic V-ATPase. *Nature*. 521:241–245.
12. Arai, S., S. Saijo, ..., T. Murata. 2013. Rotation mechanism of *Enterococcus hirae* V₁-ATPase based on asymmetric crystal structures. *Nature*. 493:703–707.
13. Suzuki, K., K. Mizutani, ..., T. Murata. 2016. Crystal structures of the ATP-binding and ADP-release dwells of the V₁ rotary motor. *Nat. Commun.* 7:13235–13244.
14. Minagawa, Y., H. Ueno, ..., R. Iino. 2013. Basic properties of rotary dynamics of the molecular motor *Enterococcus hirae* V₁-ATPase. *J. Biol. Chem.* 288:32700–32707.
15. Ueno, H., Y. Minagawa, ..., R. Iino. 2014. Torque generation of *Enterococcus hirae* V-ATPase. *J. Biol. Chem.* 289:31212–31223.
16. Iino, R., Y. Minagawa, ..., T. Murata. 2014. Molecular structure and rotary dynamics of *Enterococcus hirae* V₁-ATPase. *IUBMB Life*. 66:624–630.
17. Iino, R., H. Ueno, ..., T. Murata. 2015. Rotational mechanism of *Enterococcus hirae* V₁-ATPase by crystal-structure and single-molecule analyses. *Curr. Opin. Struct. Biol.* 31:49–56.
18. Imamura, H., M. Takeda, ..., K. Yokoyama. 2005. Rotation scheme of V₁-motor is different from that of F₁-motor. *Proc. Natl. Acad. Sci. USA*. 102:17929–17933.
19. Walker, J. E. 2013. The ATP synthase: the understood, the uncertain and the unknown. *Biochem. Soc. Trans.* 41:1–16.
20. Yasuda, R., H. Noji, ..., H. Itoh. 2001. Resolution of distinct rotational substeps by submillisecond kinetic analysis of F₁-ATPase. *Nature*. 410:898–904.
21. Mulikjanian, A. Y., K. S. Makarova, ..., E. V. Koonin. 2007. Inventing the dynamo machine: the evolution of the F-type and V-type ATPases. *Nat. Rev. Microbiol.* 5:892–899.
22. Rees, D. M., M. G. Montgomery, ..., J. E. Walker. 2012. Structural evidence of a new catalytic intermediate in the pathway of ATP hydrolysis by F₁-ATPase from bovine heart mitochondria. *Proc. Natl. Acad. Sci. USA*. 109:11139–11143.
23. Adachi, K., K. Oiwa, ..., K. Kinoshita, Jr. 2007. Coupling of rotation and catalysis in F₁-ATPase revealed by single-molecule imaging and manipulation. *Cell*. 130:309–321.
24. Bason, J. V., M. G. Montgomery, ..., J. E. Walker. 2015. How release of phosphate from mammalian F₁-ATPase generates a rotary substep. *Proc. Natl. Acad. Sci. USA*. 112:6009–6014.
25. Okazaki, K., and G. Hummer. 2013. Phosphate release coupled to rotary motion of F₁-ATPase. *Proc. Natl. Acad. Sci. USA*. 110:16468–16473.
26. Ito, Y., and M. Ikeguchi. 2015. Mechanism of the $\alpha\beta$ conformational change in F₁-ATPase after ATP hydrolysis: free-energy simulations. *Biophys. J.* 108:85–97.
27. Fiser, A., and A. Sali. 2003. Modeller: generation and refinement of homology-based protein structure models. *Methods Enzymol.* 374:461–491.
28. Foloppe, N., and A. D. MacKerell, Jr. 2000. All-atom empirical force field for nucleic acids: I. Parameter optimization based on small molecule and condensed phase macromolecular target data. *J. Comput. Chem.* 21:86–104.
29. MacKerell, A. 1997. Influence of water and sodium on the energetics of dimethylphosphate and its implications for DNA structure. *J. Chem. Phys.* 94:1436–1447.
30. Mackerell, A. D., and N. K. Banavali. 2000. All-atom empirical force field for nucleic acids: II. Application to molecular dynamics simulations of DNA and RNA in solution. *J. Comput. Chem.* 21:105–120.
31. MacKerell, A. D., D. Bashford, ..., M. Karplus. 1998. All-atom empirical potential for molecular modeling and dynamics studies of proteins. *J. Phys. Chem. B*. 102:3586–3616.
32. Mackerell, A. D., Jr., M. Feig, and C. L. Brooks, 3rd. 2004. Extending the treatment of backbone energetics in protein force fields: limitations of gas-phase quantum mechanics in reproducing protein conformational distributions in molecular dynamics simulations. *J. Comput. Chem.* 25:1400–1415.
33. Ikeguchi, M. 2004. Partial rigid-body dynamics in NPT, NPAT and NPYT ensembles for proteins and membranes. *J. Comput. Chem.* 25:529–541.
34. Jorgensen, W. L., J. Chandrasekhar, ..., M. L. Klein. 1983. Comparison of simple potential functions for simulating liquid water. *J. Chem. Phys.* 79:926–935.
35. Martyna, G. J., D. J. Tobias, and M. L. Klein. 1994. Constant pressure molecular dynamics algorithms. *J. Chem. Phys.* 101:4177–4189.
36. Essmann, U., L. Perera, ..., L. G. Pedersen. 1995. A smooth particle mesh Ewald method. *J. Chem. Phys.* 103:8577–8593.
37. de Leeuw, S. W., J. W. Perram, and E. R. Smith. 1980. Simulation of electrostatic systems in periodic boundary conditions. I. Lattice sums and dielectric constants. *Proc. Math. Phys. Eng. Sci.* 373:27–56.
38. Hummer, G., and D. M. Soumpasis. 1993. Correlations and free energies in restricted primitive model descriptions of electrolytes. *J. Chem. Phys.* 98:581–591.
39. Kenzaki, H., N. Koga, ..., S. Takada. 2011. CafeMol: a coarse-grained biomolecular simulator for simulating proteins at work. *J. Chem. Theory Comput.* 7:1979–1989.
40. Li, W., P. G. Wolynes, and S. Takada. 2011. Frustration, specific sequence dependence, and nonlinearity in large-amplitude fluctuations of allosteric proteins. *Proc. Natl. Acad. Sci. USA*. 108:3504–3509.
41. Okazaki, K., N. Koga, ..., P. G. Wolynes. 2006. Multiple-basin energy landscapes for large-amplitude conformational motions of proteins: structure-based molecular dynamics simulations. *Proc. Natl. Acad. Sci. USA*. 103:11844–11849.
42. Yao, X. Q., H. Kenzaki, ..., S. Takada. 2010. Drug export and allosteric coupling in a multidrug transporter revealed by molecular simulations. *Nat. Commun.* 1:117.
43. Okazaki, K., and S. Takada. 2008. Dynamic energy landscape view of coupled binding and protein conformational change: induced-fit versus population-shift mechanisms. *Proc. Natl. Acad. Sci. USA*. 105:11182–11187.
44. Furuike, S., M. D. Hossain, ..., K. Kinoshita, Jr. 2008. Axle-less F₁-ATPase rotates in the correct direction. *Science*. 319:955–958.
45. Baba, M., K. Iwamoto, ..., K. Yokoyama. 2016. Rotation of artificial rotor axles in rotary molecular motors. *Proc. Natl. Acad. Sci. USA*. 113:11214–11219.

46. Numoto, N., Y. Hasegawa, ..., K. Miki. 2009. Inter-subunit interaction and quaternary rearrangement defined by the central stalk of prokaryotic V_1 -ATPase. *EMBO Rep.* 10:1228–1234.
47. Maher, M. J., S. Akimoto, ..., K. Yokoyama. 2009. Crystal structure of A_3B_3 complex of V-ATPase from *Thermus thermophilus*. *EMBO J.* 28:3771–3779.
48. Nagamatsu, Y., K. Takeda, ..., K. Miki. 2013. Origin of asymmetry at the intersubunit interfaces of V_1 -ATPase from *Thermus thermophilus*. *J. Mol. Biol.* 425:2699–2708.
49. Toei, M., C. Gerle, ..., K. Yokoyama. 2007. Dodecamer rotor ring defines H^+ /ATP ratio for ATP synthesis of prokaryotic V-ATPase from *Thermus thermophilus*. *Proc. Natl. Acad. Sci. USA.* 104:20256–20261.